Journal of
Materials Chemistry A

ROYAL SOCIETY
OF CHEMISTRY

Hierarchical Tri-functional Electrocatalysts Derived from Bimetallic-imidazolate Framework for Overall Water Splitting and Rechargeable Zinc-air Batteries

SCHOLARONE™
Manuscripts

Journal of
Materials Chemistry A

ARTICLE

Hierarchical Tri-functional Electrocatalysts Derived from Bimetallic-imidazolate Framework for Overall Water Splitting and Rechargeable Zinc-air Batteries

Sung Hoon Ahn[a,b] and Arumugam Manthiram[a]*

There is a growing need for an efficient multi-functional electrocatalyst that can produce industry-level high currents at low overpotentials. Herein, we report a highly efficient, robust tri-functional catalytic electrode that simultaneously catalyzes three different electrochemical reactions: oxygen evolution reaction (OER), hydrogen evolution reaction (HER), and oxygen reduction reaction (ORR). The catalytic electrodes with a hierarchical structure are converted from a hierarchical nickel-rich, nickel-cobalt bimetallic-imidazolate framework directly grown onto a nickel foam. Catalytic electrodes composed of bimetallic phosphides exhibit excellent OER and HER catalytic activity (an overpotential of 201/250 mV at 20/100 mA cm^{-2} for OER and an overpotential of 67/110 mV at 20/100 mA cm^{-2} for HER), as well as ORR activity with a half-wave potential at 0.82 V vs. RHE. Furthermore, the bimetal-nitrogen-carbon (M-N-C) catalytic electrode also exhibits tunable tri-functional catalytic activity, including excellent ORR activity with a half-wave potential at 0.88 V vs. RHE. The high potential of these multi-functional electrocatalysts from single nickel-rich bimetallic-organic complex is demonstrated by employing them as a robust alkaline water electrolyzer, as well as the decoupled air electrodes for rechargeable zinc-air batteries (ZABs).

Introduction

The role of the electrocatalyst is central in hydrogen-based energy conversion and storage systems.[1-3] However, the high cost and low efficiency of the electrochemical devices is a major challenge in building a commercial clean energy conversion and storage system. In addition, the use of different single-functional catalysts for each electrode of an electrochemical device further reduces the cost-efficiency of devices requiring two or more electrochemical redox reactions. Therefore, by introducing catalysts with two or more catalytic activities in the same electrolyte, the manufacturing process of the catalytic electrode as well as the system itself can be simplified to increase the cost-efficiency. Catalytic electrodes with bi-functional activity have been developed particularly for the overall water splitting and the rechargeable zinc-air batteries. For example, an overall water electrolyzer consists of two electrodes for a hydrogen evolution reaction (HER) and an oxygen evolution reaction (OER),

whereas a rechargeable zinc-air battery requires an oxygen evolution and an oxygen reduction reaction (ORR).

By screening some catalyst candidates with experimental and theoretical study such as density-functional theory (DFT),[4,5] some catalytic active sites are proven to have bi-functional activity toward OER/HER for an overall water splitting, or toward OER/ORR for rechargeable zin-air batteries. Electrocatalysts containing two or more metal elements have a much higher single catalytic activity than single metal-based one[6-8], and metal oxides such as perovskite structures have been reported to have high bi-functional catalytic activity.[9,10] In the other way, the coordination of metals and organic elements can be used to achieve multiple catalytic activity. Metal chalcogenides (M-X, X = S, P, Se) have been reported to have excellent bi-functional catalytic activity for OER and HER[11-15]. In addition, a carbon material doped with one or more organic elements (N, S, P, B) and a metal-carbon composite material comprising a transition metal and nitrogen-doped carbon may also have multiple catalytic activities.[16-18] The bi-functioanl electrocatalysts have been applied to electrodes for alkaline water electrolyzer and rechargeable zinc-air batteries to demonstrate the potential to improve the cost effectiveness of the system. Despite considerable progress in the development of bifunctional electrode catalysts, there are only a few reports of tri-functional electrocatalysts with high catalytic activity and durability for the three different electrochemical reactions: oxygen evolution reaction (OER), hydrogen evolution reaction (HER), and oxygen reduction reaction (ORR). Some catalytic materials such as transition-metal oxyhydroxides,[19] metal-free carbon catalysts,[20-22] and metal-carbon composite materials,[23,24] and metal chalcogenides[25,26] have been reported to have tri-functional catalytic activity. However, in most

[a] Prof. S. H. Ahn, Prof. A. Manthiram, Materials Science and Engineering Program, Texas Materials Institute,The University of Texas at Austin, Austin, Texas 78712, USA.

[b] Prof. S. H. Ahn, Department of Bio-chemical and Polymer Engineering Chosun University, Gwangju, 501-759, Republic of Korea

*E-mail: manth@austin.utexas.edu; Fax: +1-512-471-7681; Tel: +1-512-471-1791

†Electronic Supplementary Information (ESI) available. See DOI: 10.1039/x0xx00000x
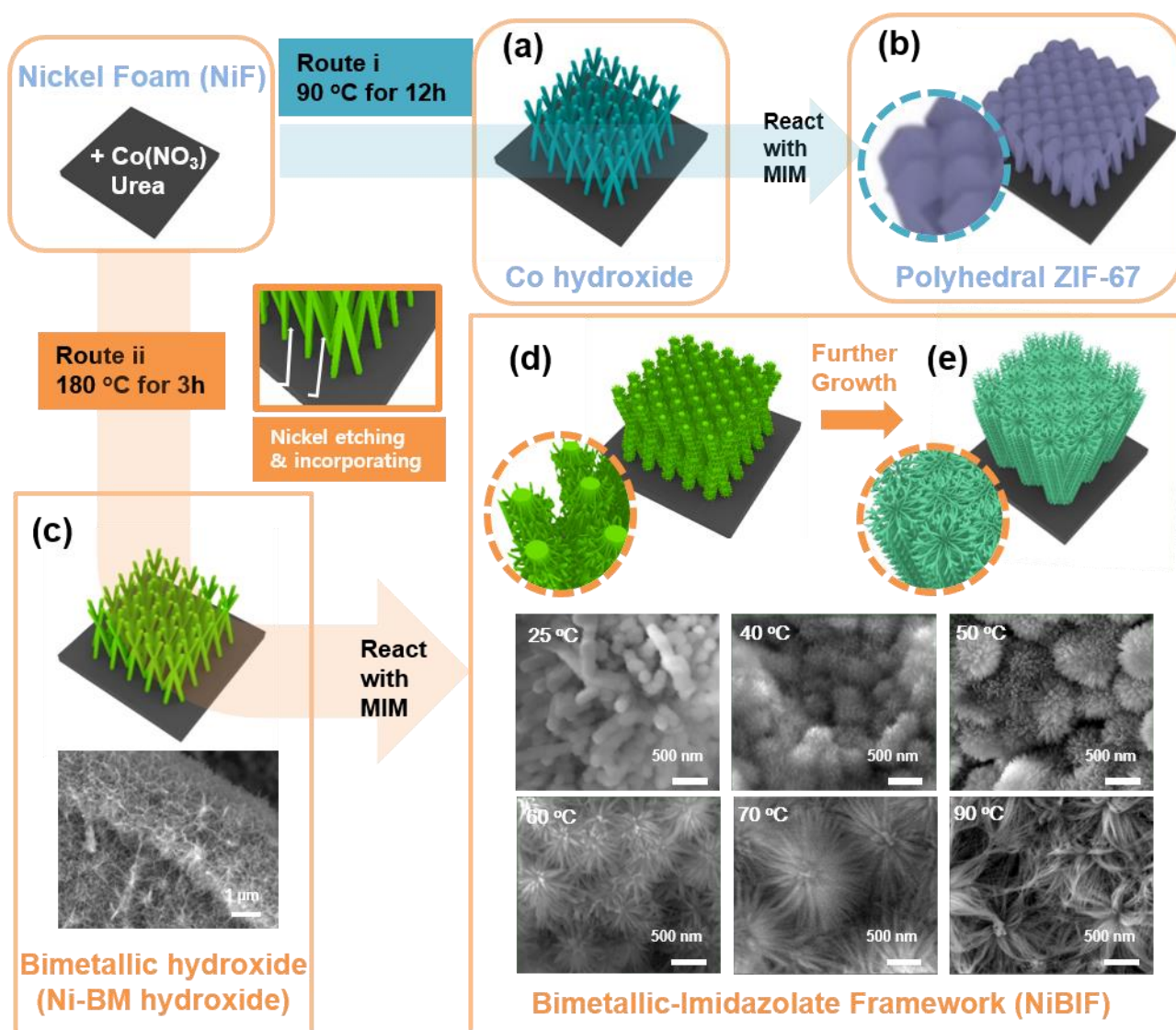
Figure 1. A schematic illustration of the two-step sequential reactions for the synthesis of two types of metal-imidazolae framework electrodes. In route (i), (a) the cobalt hydroxide nanostructure is reacted with the 2-methylimidazole (MIM) solution and converted to (b) the polyhedral ZIF-67 electrode. In the route (ii), (c) the nickel-rich bimetallic hydroxide nanostructure is used as a solid precursor and is converted to (d) a nickel-rich bimetallic imidazolate framework electrode. (e) By adjusting the reaction temperature and time, the size and interconnectivity of NiBIF can be increased.

cases the reported tri-functional activity was not comparable to the single-functional catalytic activity of the benchmark catalysts. In addition, the complicated and time-consuming manufacturing process made it difficult to mass produce the catalytic electrodes.

To produce multi-functional electrocatalysts, metal-organic framework (MOF) has also been regarded as the most promising platform. Due to the complex chemical composition of the various metal and organic structures, MOF can be directly converted to versatile electrocatalysts. The metal or organic element may be selectively removed to produce the metal derivatives including metal (oxy)hydroxide, to produce a metal-free carbon material, or it can converted to metal-carbon complex materials. Some typical subclasses of MOF, such as prussian blue[27] and zeolitic imidazole framework (ZIF),[28, 29] have been studied for the bi-functional electrocatalysts toward overall water splitting and rechargeable zinc-air batteries. In particularly, the basic structural units of ZIF materials are composed of metal ions coordinated by benzyl-imidazole rings, which allows them to be converted to various nitrogen-doped carbon-containing electrocatalysts. As a result, ZIF-based synthesis methods have received great interest as highly promising candidates for producing non-precious electrocatalyst, because it can produce not only excellent HER and OER catalysts, but also ORR electrocatalysts from a single ZIF material.[30] Despite the high potential of ZIF materials, the specific activity of electrocatalyst are still not satisfactory in the practical applications of water electrolyzer and zinc-air batteries. One of the most challenging problems is to produce them in close contact between the ZIF-derived materials and the substrate electrode. The voids between the catalyst material

and the electrode induces interfacial resistance. Considering the industrial scale of the water electrolyzer for hydrogen production, which requires a high current density of 200 - 400 mA cm^{-2} at 1.8-2.4 V,[31] considerable additional overpotential is required to compensate the iR drop. For this reason, attempts have been made to grow ZIF-derived catalytic materials directly from the electrode substrate.[32] However, the catalytic electrode derived from ZIF-67 is still composed of polyhedral structure, and the catalytic activity is not sufficient for industrial-scale hydrogen production.

In this study, we report highly efficient and robust tri-functional catalytic electrodes with a novel solid metal precursor-based synthesis process.[33] This process allows direct growth of a catalyst material on a nickel foam with a hierarchical nanostructure, which is completely different from a typical polyhedral ZIF nanocrystal. The catalytic electrode was applied to alkaline water electrolyzer and rechargeable zinc-air batteries. In the two-step synthesis process, bimetal hydroxide with nanowire structure are firstly grown directly on nickel foam, and then converted to a bimetallic-imidazolate framework with a hierarchical structure by reaction with 2-methylimidazole. This hierarchical structure of bimetallic-imidazolate framework is combined with detailed core-shell nanostructures to produce synergistic effects. In the presence of such a framework composed of bimetals and imidazolate, the catalyst nanoparticles are successfully encapsulated within a nitrogen-doped carbon shells through an annealing process. As a result, the catalytic electrode grown directly on the nickel foam exhibits robust catalytic performance for a variety of electrochemical reactions. Catalytic electrodes composed of bimetallic phosphides exhibit excellent OER and HER catalytic performances (an overpotential of 201/250 mV at 20/100 mA cm^{-2} for OER and an overpotential of 67/110 mV at 20/100 mA cm^{-2} for HER) and ORR catalytic performance with a half-wave potential at 0.82 V vs. RHE. Furthermore, the bimetal-nitrogen-carbon (M-N-C) catalytic electrode also exhibits tunable tri-functional catlytic activity including excellent ORR performance with a half-wave potential at 0.88 V vs. RHE. This tri-functional catalyst activity overwhelms that of the benchmark single-functional catalyst for each reaction.

To demonstrate their high catalytic properties and durability, these catalytic electrodes are then applied in alkaline water electrolyzers and rechargeable ZABs. An alkaline water electrolyzer composed of symmetric electrodes is proven to produce high current densities with extremely low overvoltage (1.46/1.65 V vs. RHE at a current density of 10/100 mA cm^{-2}) with high durability. Rechargeable zinc-air batteries with these highly active and durable catalytic electrodes also exhibit low initial charge-discharge overpotentials at 10 mA cm^{-2} in a cycling test of over 210 h. The production of efficient electrocatalysts using these abundant and inexpensive raw materials is expected to greatly accelerate the commercialization of many energy conversion and storage systems that require an electrocatalyst.

Herein, we report a rational design of carbon-incorporated porous Ni-Fe phosphide nanorods directly grown onto commercial nickel foam and its direct use as a water splitting catalyst without the addition of a polymeric binder. Bimetallic Ni-Fe nanorods composed of metal-organic framework are converted from NiFe nanoflakes, which serve as the metal source in the presence of organic ligands

via a hydrothermal reaction. The Ni-Fe MOF nanorods are subsequetly converted to porous Ni-Fe phosphide nanorods after a low-temperature phosphidation process. The porous Ni-Fe phosphide nanorods exhibit prominent catalytic activities toward both HER and OER in 1 M KOH alkaline solution. As an integrated water electrolyzer for overall water splitting composed of a two-electrode setup in alkaline solution, this device needs only 1.52 V to afford 10 mA cm^{-2} current density with excellent long-term stability. Such a remarkable overall water splitting activity can be ascribed to its direct contact to the three-dimensional (3D) substrate as well as the MOF-derived benefits in carbon-incorporated highly organized nanostructure with a number of efficient Ni-Fe-P active sites.

Experimental Section

Materials Synthesis

Synthesis of nickel-rich bimetallic hydroxide nanowires (NiBM hydroxide): First, 0.1 M of cobalt nitrate hexahydrate (CoNO$_3$ · 6H$_2$O) and 0.25 M urea were dissolved in 80 mL of deionized water (DI water), and then magnetically stirred for 30 minutes. A commercial nickel foam (1.5 x 6 cm) was then cleaned by ultrasonication in acetone and deionized water for 30 minutes. The clear solution and the two nickel foams were transferred to a 100 mL Teflon-lined autoclave and placed in an electric oven at 180 ^{o}C for 3 h. After cooling naturally, the product on the nickel foam was washed twice with deionized water and dried at 50 ^{o}C overnight. The precipitated powder was also collected by vacuum filtration, washed twice with deionized water, and dried at 50 °C.

Synthesis of nickel-rich bimetallic-imidazolate framework (NiBIF): The as-prepared NiBM hydroxide on nickel foam was cut into the size of 1.5 X 3 cm and transferred to a 20 mL glass vial. 10 mL of 10 wt.% 2-methylimidazole (MIM) aqueous solution was poured into the glass vial and then placed in an electric oven at the desired temperatures[32, 34, 35] (25, 40, 50, 60, 70, 80 and 90 ^{o}C) for 8 h. To investigate the mechanism of the conversion reaction, the NiBIF samples were collected after the reaction times of 2, 4, and 8 h at 40 ^{o}C (or 2, 4 ,8, and 12 h for at 50 ^{o}C) and the surface was analyzed by SEM. To prepare the powder-type NiBIF, 0.5 g of NiBM hydroxide was reacted in 10 mL of 10 wt.% MIM aqueous solution at the desired temperatures for 8 h.

Synthesis of NiBM-O, NiBM@N$_x$C, NiBMP@N$_x$C: NiBM-O was produced by an annealing process at 350 ^{o}C for 3 h in air. *NiBM@N$_x$C* was produced by an annealing process under argon at 800 ° C for 3 h at a ramp rate of 5 ° C min$^-$. In the process to prepare NiBMP@N$_x$C, two pieces of NiBIF were placed in a graphite boat, and 0.5 g of NaH$_2$PO$_2$·H$_2$O was placed in a separate graphite box and positioned upstream of an argon flow. NiBMP@N$_x$C was obtained by an annealing process at 350 ° C for 2 h in an argon atmosphere, followed by a further annealing process in an argon flow at 700 ^{o}C for 3 h.

Synthesis of NiBM@N$_x$C powder: To obtain NiBM@N$_x$C powder, the as-prepared NiBIF precipitate was annealed under argon at 800 ° C for 3 h at a ramp rate of 5 ° C min^{-1}.

Catalytic ink preparation: 10 mg of NiBM@N$_x$C or Pt / C catalyst (20 wt % on Vulcan XC-72, ETEK) was dispersed in 1950 μL of isopropanol and 50 μL of Nafion solution (5 wt.%) to prepare a homogeneous black ink solution by ultrasonication for 1 h.

ARTICLE   **Journal of Materials Chemistry A**

Electrochemical analysis

Electrochemical Analysis toward OER / HER:

Electrochemical analysis was performed with a potentiostat (ZIVE BP2C) and a conventional three-electrode configuration with the as-prepared catalytic electrode as a working electrode, platinum mesh as a counter electrode, and mercury/mercury oxide (Hg/HgO, NaOH (1M)) as a reference electrode. The potential versus reversible hydrogen electrode (E_{RHE}) was converted from the potential versus Hg/HgO following the Nernst equation:

$$E_{RHE} = E_{Hg/HgO} + 0.059 \times (pH) + 0.14 \qquad (1)$$

The linear sweep voltammetry (LSV) curves were obtained in N_2 saturated 1 M KOH solution at 1 mV s^{-1}. The stability of the catalysts for overall water splitting was evaluated by the chronoamperometry analysis at 1.47 and 1.65 V for 30 h. The electrochemical surface area (ECSA) was determined by measuring the capacitive current associated with double-layer charging from the scan rate dependence of cyclic voltammetry (CV). CV was recorded in the potential range between 0.92 to 1.02 V_{RHE} at scan rates of 10 – 100 mV s^{-1}. The double-layer capacitance (C_{dl}) was estimated by plotting the current density variation, $\Delta J = (J_a - J_c)$ at 1.20 V_{RHE}. The linear slope is twice that of the double-layer capacitance. Electrochemical impedance spectroscopy (EIS) measurements were recorded with a ZIVE BP2C (Wonatech, Korea) workstation in the frequency range of 10^6 to 10^{-1} Hz with an amplitude perturbation of 5 mV.

Rotation disk experiment (RDE) and rotating ring-disk experiment (RRDE): 16 μL of the as-prepared carbon catalyst ink was deposited onto a glassy carbon electrode with a diameter of 5 mm to make a loading amount of ~ 0.4 mg cm^{-2}. Prior to the electrochemical analysis, 0.1 M KOH electrolyte was saturated with oxygen by bubbling O_2 gas for 30 minutes. Electrochemical analysis was performed with a potentiostat (Autolab PGSTAT302N) and a rotation controller (Pine Research Instrumentation) based on a conventional three-electrode configuration consisting of a glassy carbon electrode as the working electrode, a platinum mesh as the counter electrode, and a Hg/HgO electrode as the reference electrode. Cyclic voltammetry (CV) analysis was performed at a scan rate of 5 mV s^{-1} in O_2 saturated 0.1 M KOH solution. Linear sweep voltammetry (LSV) curves were obtained in O_2 saturated 0.1 M KOH at different speed rates from 400 to 2400 rpm at 1 mV s^{-1}. The durability of the electrocatalyst was evaluated by continuous 10,000 potential cycles from 0.6 to 1.0 V_{RHE} with a triangle wave at 50 mV s^{-1} in O_2-saturated 0.1 M KOH electrolyte.

The kinetics parameters during ORR were determined according to the Koutecky–Levich equation given below:

$$\frac{1}{J} = \frac{1}{J_L} + \frac{1}{J_K} = \frac{1}{B\omega^{1/2}} + \frac{1}{J_K} \qquad (2)$$

$$B = 0.62nFC_0(D_0)^{2/3}\nu^{-\frac{1}{6}} \qquad (3)$$

where J is the measured current density at a specific potential, J_K is the kinetic current density, J_L is the diffusion-limited current density, ω is the electrode rotation speed, F is the Faraday constant (F = 96485 C mol^{-1}), C_0 is the bulk concentration of O_2 (1.2 × 10^{-3}mol cm^{-3}) for both 0.1 M KOH; D_0 is the diffusion coefficient of O_2 (1.9×10^{-5} cm^2 s $^{-1}$ for 0.1 M KOH solution) and ν is the kinetic viscosity of the electrolyte (0.01 cm^2 s $^{-1}$ for 0.1 M KOH solution). The electron transfer number was obtained from the slope of the K-L plot. RRDE

tests were carried out in O_2 saturated 0.1 M KOH solution at 1,600 rpm with a scan rate of 1 mV s^{-1}, and the potential of the Pt ring was set at V = 1.3 V_{RHE}. The electron transfer number (n) and the yield of hydrogen peroxide released during ORR was calculated based on the following equation,

$$n = 4 \times \frac{I_D}{I_R/N + I_D} \qquad (4)$$

$$\% H_2O_2 = 200 \times \frac{I_R/N}{I_R/N + I_D} \qquad (5)$$

where I_D is the disk current, I_R is the ring current, and N is the collection coefficient of the Pt ring (N = 0.37)

Rechargeable Zinc-air battery test

The rechargeable zinc-air battery tests were carried out with a home-made PTFE layered battery mold. The decoupled configuration of the non-precious metal catalyst based ZABs consisted of NiBM@N$_x$C ORR electrodes and NiBMP@N$_x$C OER electrodes fabricated from two pieces of NiBIF grown directly on nickel foam. To prepare the precious-metal catalyst air electrodes, the ORR electrode was prepared by the deposition of Pt/C catalyst onto hydrophobic carbon nanofiber paper (CNF) (0.75 x 0.75 cm^2) with a mass loading of ~ 2 mg cm^{-2}, while the OER electrode was prepared by the deposition of Ir/C catalyst (20 wt% on Vulcan XC-72, Premeteck) on a nickel foam with a mass loading of ~ 2 mg cm^{-2}. A polished zinc plate was used as an anode and the electrolyte was 6 M KOH with 0.2 M ZnCl$_2$ solution. The cycling performance of the ZABs was evaluated with two independent channels of the Arbin 2000 battery cycler at a current density of 10 mA cm^{-2} in ambient air. Each charge and discharge period was set to 2 h.

Results and discussion

In Fig. 1, the overall nickel-rich bimetallic-imidazolate framework synthesis process with the subsequent two-step reactions are illustrated. For route i, cobalt oxyhydroxide nanowires (Co hydroxide, Fig. 1a) were first directly grown onto nickel foam by hydrothermal reaction at 90 °C for 8 h. In the following second-step to produce bimetallic-imidazolate framework, the pre-designed metal oxyhydroxide was used as a solid precursor, and then reacted with an organic linker[33]. In this step, Co hydroxide was immersed into 10 wt.% 2-methylimidazole aqueous solution at 60 °C for 12 h to convert to ZIF-67 coated onto nickel foam(ZIF-67, Fig. 1b). However, when the reaction progressed fully, the ZIF-67 nanoparticles eventually became larger and the polyhedral structure was generated. The color of the sample turned from light pink to blue, which is the typical color of ZIF-67 nanocrystals. In the case of route ii, the hydrothermal reaction was carried out in conditions identical to route i, except for the reaction temperature, which was 180 °C to obtain nickel-rich bimetallic hydroxide (NiBM hydroxide, Fig. 1c). During the hydrothermal reaction, nickel species from the nickel foam substrate were etched and dissolved at high temperature, and *in-situ* incorporated into the nanowires to produce nickel-rich nickel-cobalt oxyhydroxide nanowires. The formation of a nickel-rich surface on the NiBM hydroxide is a key factor for the formation of nickel-rich bimetallic-imidazolate framework material with a controlled nanostructure. After the subsequent simple treatment, hierarchical nickel-rich bimetallic-imidazolate framework was successfully produced (NiBIF, Fig. 1d). The color of the NiBIF at this point was yellow-green, indicating the successful formation of a nickel-based
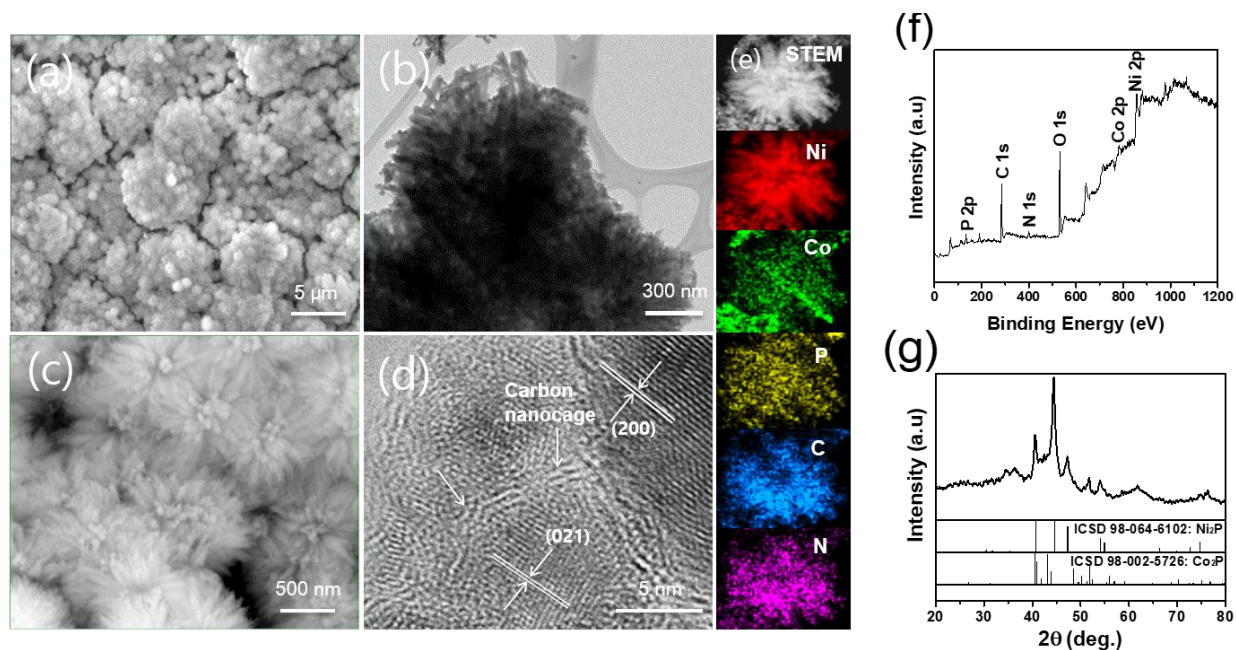
Figure 2. (a, c) SEM images, (b) TEM image, and (d) HR-TEM image of NiBMP@N$_x$C. (e) STEM and corresponding elemental mapping images for Ni, Co, P, C, N of NiBMP@N$_x$C. (f) XPS survey spectra and (g) XRD pattern of NiBMP@N$_x$C.

complex. Pictures showing the colors of the NiBIF at different temperatures are illustrated in Fig. S1, and the comparison between ZIF-67 and NiBIF is shown in Fig. S2.

The synthetic mechanism and the two-step process were investigated by observing the various conversion processes for the NiBIF samples. The reaction temperature in the second-step conversion reaction was systematically controlled to investigate the nucleation and growth mechanism of the NiBIF nanocrystals. As illustrated in Fig. 1d, as the reaction temperature increased, the formation of NiBIF nanocrystals was promoted and the sizes of the flower-like NiBIF nanocrystals also increased. More detailed nanostructure can be observed in the scanning electron microscopy (SEM) images in Fig. S3 and S4. The starting NiBM hydroxide nanowires (Fig. S3a,e) were processed for the conversion to NiBIF samples, and the reaction temperature in the second-step process was controlled at 25 °C (Fig. S3b,f), 40 °C (Fig. S3c,g), 50 °C (Fig. S3d,h), 60 °C (Fig. S3a,e), 70 °C (Fig. S4b,f), 80 °C (Fig. S4c,g) and 90 °C (Fig. S4d,h) for 8 h, respectively. As the reaction progressed at the high temperature, the growth of NiBIF nanoparticles accelerated and their size increased. For the NiBIF treated at 25 °C, the shape of the nanowires that were not completely converted to NiBIF could be observed (Fig. S5a,b).

To further investigate the growth mechanism of the NiBIF on the surface of nanowires, the samples processed at 40 and 50 °C were observed over time (Fig. S6 and S7, respectively). In the early stages of the reaction at 40 °C (Fig. S6a,d) or 50 °C (Fig. S7a,e), it was observed that NiBIF nanocrystals were formed on the surface of some nanowires. As the reaction progressed, the nanocrystals grew larger in size and further developed into a flower-like morphology (Fig. S6b,e and Fig. S7b,f). Consequently, the hierarchical NiBIF were

fully developed and interconnected with each other (Fig. S6c,f and Fig. S7d,h). Fourier-transform infrared spectroscopy (FT-IR, Fig. S8a), Powder X-ray Diffraction (PXRD, Fig. S8b), and X- photoelectron ray spectroscopy (XPS, Fig. S9) analyses were carried out to confirm the chemical composition of the NiBIF and to confirm the coordination of the organic ligand with the bi-metals. First, when compared to the original FT-IR spectra of 2-methylimidazole (MIM) in Fig. S8a, a new adsorption peak at 426 cm^{-2} appeared in the ZIF-67 sample, which represents the metal-nitrogen stretching vibration.[36] Similarly, NiBIF showed an additional peak of 406 and 474 cm^{-2}, indicating the coordination between the nickel/cobalt metals and the organic linkers in the NiBIF. Both of the ZIF-67 and NiBIF nanomaterials showed a significant decrease in the broad peak between 2200 and 3400 cm^{-2}, indicating the deprotonation of the N-H groups of the MIM ligands upon coordination with the metal ions.[37] In the PXRD analysis in Fig. S8b, the two ZIF-67 and NiBIF samples showed no significant difference in the PXRD pattern, indicating the successful formation of bimetallic-imidazolate complex. Finally, in the XPS spectra (Fig. S9), it was confirmed that nickel and cobalt were present simultaneously in the NiBM hydroxide (Fig. S9a) and NiBIF (Fig. S9b) samples, which can be attributed to the *in-situ* incorporation of nickel species from the nickel foam substrate during the 180 °C hydrothermal reaction. On the other hand, only cobalt peaks were observed for the Co hydroxide (Fig. S9c) and ZIF-67 (Fig. S9d). Note that in these three analyses, powder-type samples were detached from the nickel foam by intensive ultrasonic treatment to avoid any interference with the nickel substrate signal. As confirmed in Fig. S9d, NiBIF contains a wide variety of functional elements including nickel, cobalt, nitrogen and carbon. This allows it to easily convert to various bi-metallic derivatives coupled with N-doped carbonaceous
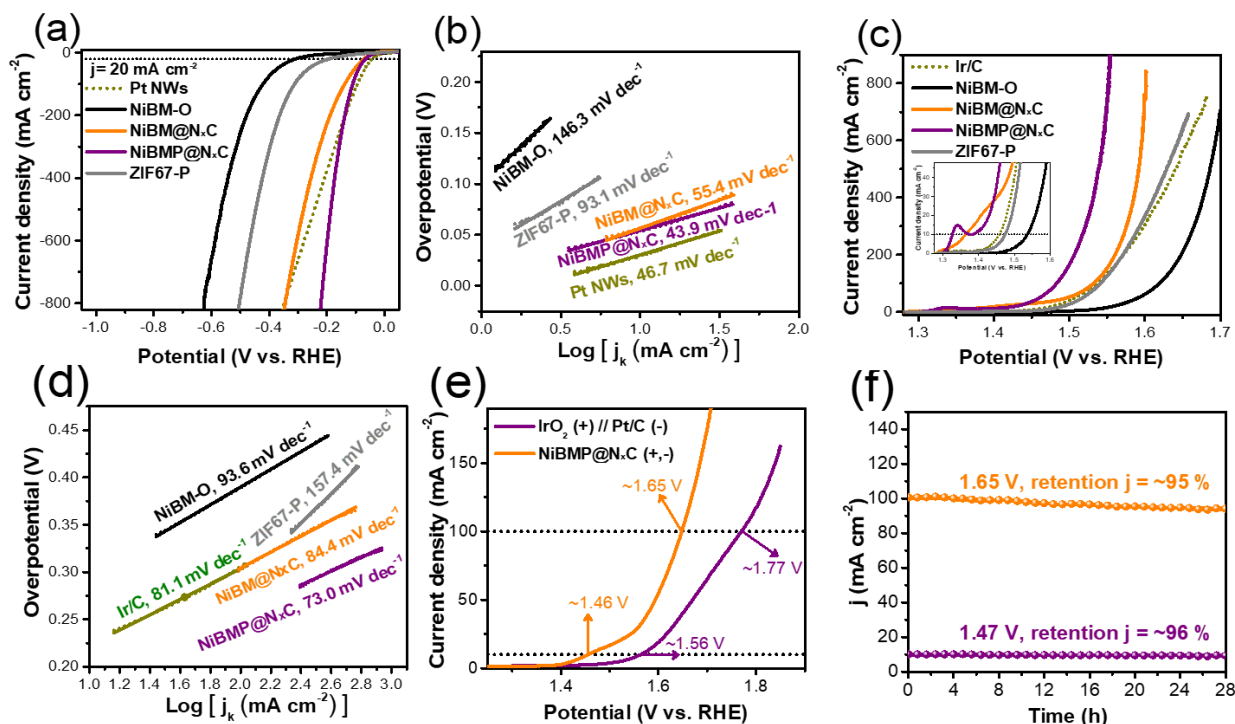
Figure 3. (a) Polarization curves of the various metal-imidazole framework-based catalysts and Pt/C for HER in 1 M KOH solution, (b) corresponding Tafel plots derived from panel (a). (c) Polarization curves of the various metal-imidazole framework-based catalysts and Ir/C for OER in 1 M KOH, (d) corresponding Tafel plots derived from panel (c). e) Polarization curves of Ir/C // Pt/C and a symmetric NiBMP@N_xC water electrolyzer for overall water splitting. (f) Chronoamperometry result of NiBMP@NxC water electrolyzer with an applied potential at 1.47 and 1.65 V in 1 M KOH electrolyte.

materials after an annealing treatment under an inert atmosphere. In the presence of a bimetallic-imidazolate framework, the multimetal catalytic nanoparticles could be successfully encapsulated by a few layers of graphitic carbon shells. Note that typical NiBIF samples processed at 60 °C (Fig. S10a,c) were chosen to produce the bimetallic derivatives. First, NiBIF electrode was converted to metal oxides by heat treatment at 350 ° C for 3 hours in an air atmosphere (denoted NiBM-O). Next, the NiBIF electrode was subjected to an annealing process at 800 °C in an argon atmosphere to prepare carbon-mixed metal-carbon composite catalysts (denoted NiBM@N_xC, Fig. S10c,f). Finally, a bimetallic phosphide complex was prepared by an two-step annealing process with a phosphorus source in an argon atmosphere (denoted as NiBMP@N_xC, Fig. 2a,c). It was confirmed that after these subsequent treatments the samples retained the original hierarchical structure of the NiBIF. The detailed structure of NiBMP@N_xC was observed with transmission electron microscopy (TEM) to investigate the effect of the well-arranged carbon elements in the metal-imidazolate framework on the formation of the carbon matrix in the NiBMP@N_xC complexes (Fig. 2b). As shown in the high-resolution TEM image (HR-TEM, Fig. 2d), nickel-cobalt phosphide catalytic nanoparticles with a size of several nanometers were encapsulated by a few layers of the graphitized carbon nanocages. The encapsulated nanoparticles showed clear lattice fringes with an interplanar distance of 0.253 nm, which corresponds to the (200) planes of NiCoP, as well as an

interplanar distance of 0.21 nm, which corresponds to the (211) planes of Ni_2P.[38] The scanning transmission electron microscopy (STEM) image and energy dispersive X-ray spectroscopy (EDS) elemental mapping images in Fig. 2e indicated a uniform distribution of Co, Ni, P, C and N in the flower-like single nanocrytal. The XPS survey spectra of NiBMP@N_xC (Fig. 2f) also confirms the existence of these elements. The high resolution XPS spectra of Ni, Co, P in NiBMP@N_xC are shown in Fig. S11a, b, and c, respectively. More specifically, the fine Ni 2p spectra shows the peak around 852.9 eV assigned to Ni-P bond and around 856.3 eV for the oxidized nickel species.[37] Similarly, the Co 2p spectra also shows two peaks around 781.1 and 783.7 eV, which are attributed to the Co-P bond and oxidized cobalt species, respectively.[39] For P 2p, there are peaks around 129.6 eV reflecting the binding energy of P 2p and around 133.2 eV for oxidized P species.[40] The atomic ratio of each element obtained from the EDS, XPS, and inductively coupled plasma (IPC) analyses are shown in Table S1. The PXRD pattern in Fig. 2g shows that the crystalline phase of NiBMP@N_xC is composed of Ni_2P (ICSD No. 98-064-6102) and Co_2P (98-002-5726), with Ni_2P as the major component. Thin-film XRD patterns were also collected from NiBMP@N_xC, as shown in Fig. S12. Despite a relatively strong nickel peak from the nickel foam substrate, a similar XRD pattern was observed. A control sample of ZIF-67 was also prepared by the two-step reactions, first by the growth of the cobalt hydroxide nanowires, followed by the ZIF conversion process at 60 °C. As reported in the
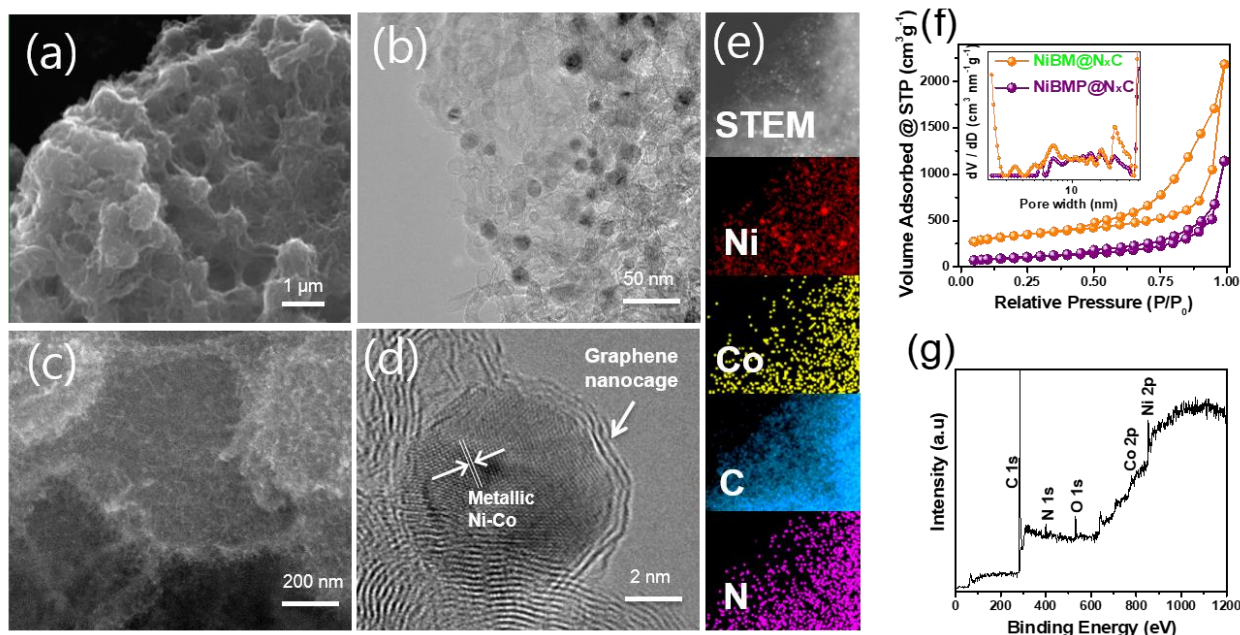
Figure 4. (a, c) FE-SEM images, (b) TEM image, and (d) HR-TEM image of NiBM@N$_x$C. (e) STEM image and corresponding elemental mapping images for Ni, Co, C and N. (f) N$_2$ isotherms and pore size distribution (inset) of NiBMP@N$_x$C and NiBM@N$_x$C and (g) XPS survey spectra of NiBM@N$_x$C.

literature about the post-conversion of the Co nanostructure to ZIF-67,[32] the nanostructure of the cobalt hydroxide nanowires (Fig. S13a,d) was successfully converted to ZIF-67 with a typical polyhedral shape (Fig. S13b,e), and the morphology was preserved after the phosphidation process (denoted ZIF-67-P, Fig. S13c,f).

Encouraged by the unique hierarchical nanostructures and uniform distribution of the elements of the NiBIF, next the electrochemical properties of the NiBIF-derived catalysts were investigated. In Fig. 3a, the catalytic activities of NiBM-O, NiBM@N$_x$C, NiBMP@N$_x$C, ZIF-67-P, and Pt/C (20 wt.% Pt on Vulcan XC-72) for HER were evaluated in 1 M KOH solution with linear sweep voltammetry(LSV) at a scan rate of 1 mV s^{-1}. First, the NiBM-O required an overpotential of 309 mV to generate 20 mA cm^{-2} of current density (and η =422 mV at 100 mA cm^{-2}) for HER. The catalytic activity was greatly enhanced for the NiBM@N$_x$C by an introduction of nitrogen-doped carbon nanocages with an overpotential at 71 at 20 mA cm^{-2}, and at 134 mV at 100 mA cm^{-2} current density compared to that of NiBM-O. Finally, the NiBMP@N$_x$C in particular exhibited only 67 mV of overpotential at 20 mA cm^{-2}, and required an additional 47 mV to achieve 100 mA cm^{-2}, indicating an extremely robust HER activity and comparable to that of the Pt/C catalyst (η=46 mV at j=20 mA cm^{-2}, and η =114 mV at j=100 mA cm^{-2}). However, the catalytic activity of ZIF-67-P (η=193 mV at j=20 mA cm^{-2}, and η =314 mV at j=100 mA cm^{-2}) was much inferior to that of the NiBM@N$_x$C and NiBMP@N$_x$C. As shown in Fig. 3b, the Tafel slope of NiBMP@N$_x$C was 43.9 mV dec^{-1}, which is the smallest value compared to that of NiBM@N$_x$C (55.4 mV dec^{-1}) and NiBM-O (146.3 mV dec^{-1}), ZIF-67-P (93.1 mVdec^{-1}), as well as Pt/C catalyst (46.7 mV dec^{-1}).

In Fig. 3c, the OER catalytic activity of the 4 catalytic electrodes noted above, and Ir/C (20 wt.% Ir on Vulcan XC-72), was also evaluated in 1

M KOH solution. Note that the catalyst was activated and stabilized for 50 cyclic voltammetry (CV) cycles prior to measuring the catalytic activity. In the case of NiBM-O, ~ 340 mV of overpotential was needed to generate 20 mA cm^{-2} current density for OER. The catalytic activity of NiBM@N$_x$C was improved with a significant shift in the LSV curve to the anodic direction in the presence of carbon matrix. Finally, NiBMP@N$_x$C, where bimetallic phosphors are supported by N-doped carbon matrix, required an overvoltage of 201 mV to generate j = 20 mA cm^{-2} for OER. Again, only an additional 53 mV of overpotential was needed to generate j=100 mA cm^{-2}. The Ni$^{2+/3+}$ redox peaks of NiBM@N$_x$C and NiBMP@N$_x$C observed in the inset image of Fig. 3c can be explained to be due to the possibility of reaching the nickel active site in the presence of a high conductivity carbon matrix[41, 42]. The exhibited bi-functional activity of NiBMP@N$_x$C toward both HER and OER were significantly superior to the results for other state-of-the-art catalysts in alkaline solutions for overall water splitting(Table S2).[17, 27, 43-47] The kinetic activity of the catalyst was also estimated and presented in a Tafel plot(Fig. 3d). The NiBMP@N$_x$C bulk electrode exhibited favorable kinetics toward the OER with the smallest Tafel slope of 73.0 mV dec^{-1}. Since catalytic activity can be affected by its nanostructure, the HER activity (Fig. S14a) and the OER activity (Fig. S14b) of the various NiBMP@N$_x$C electrodes with different nanostructures were also evaluated.

To investigate the origin of the prominent catalytic activity of NiBMP@N$_x$C, electrochemical analyses were carried out for the catalytic electrodes. Nyquist plots from electrochemical impedance spectroscopy (EIS) at the potentials in the HER region (Fig. S15a) and in the OER region (Fig. S15b) are illustrated for 4 samples. By comparison, NiBMP@N$_x$C exhibited very small charge transfer resistance (R$_{ct}$) as well as the sheet resistance (R$_s$) among the 4
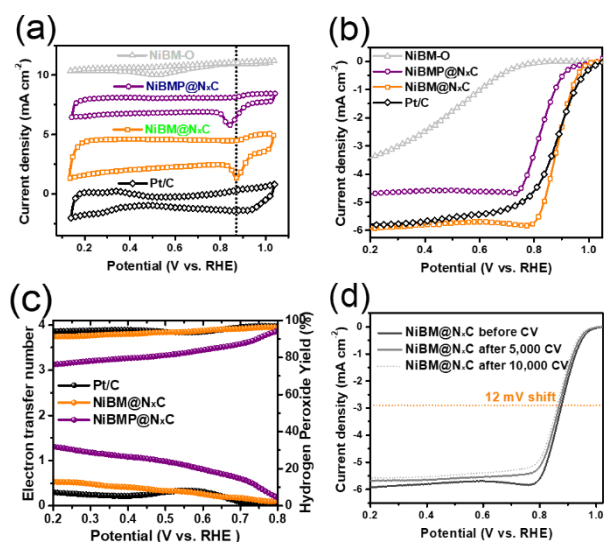
Figure 5. (a) CV curves of NiBM-O, NiBM@N$_x$C, NiBMP@N$_x$C, and Pt/C in O$_2$ saturated 0.1 M KOH electrolyte. (b) LSV curves of the as-prepared NiBIF-derived catalysts and Pt/C in O$_2$-saturated 0.1 M KOH electrolyte at a rotation speed of 1600 rpm, (c) peroxide yield and electron-transfer number of the NiBMP@N$_x$C, NiBM@N$_x$C catalysts and Pt/C catalyst at various potentials based on the RRDE data. (d) LSV curves of NiBM@N$_x$C before (dark gray line) and after 5,000 (gray line) cycles and after 10,000 cycles (dotted light gray line) from 0.6 V$_{RHE}$ to 1.0 V$_{RHE}$ in 0.1 M KOH electrolyte at 50 mV s^{-1}.

samples for both HER and OER, indicating very favorable electrochemical reaction kinetics for overall water splitting. Similarly, smaller R_{ct} and R_s values were observed for the NiBMP@N$_x$C electrodes with different nanostructures (Fig. S15c, d). However, for the NiBM hydroxide sample without the conversion reaction (displayed as untreated), both the R_{ct} and R_s values were significantly higher than those for the NiBMP@N$_x$C samples. From these results, it is expected that the monolithic nature of the synthesized bulk electrode induces good electrical contact and favorable electrochemical reaction. In addition, the hierarchy of carbon nanocages encapsulating the catalyst nanoparticles produced in the presence of metal-imidazolate framework synergistically support ideal electron transport and catalytic kinetics. The electrochemical surface area (ECSA) of the samples was also estimated by sequential CV analyses at various scan rates (Fig. S16a,b). The C_{dl} values of the catalytic electrode were calculated from the capacitive currents in the CV curves as a function of the scan rate (Fig. S17). The NiBMP@N$_x$C electrode had a higher C_{dl} of about 59.6 mF cm^{-2}, which is about 2.26 times higher than that of ZIF-67-P (23.3 mFcm^{-2}) and is attributed to the hierarchical core-shell composite structure of NiBMP@N$_x$C, as compared to the polyhedral structure of ZIF-67-P. The high ECSA of the NiBMP@N$_x$C electrode indicates that the penetration of the electrolyte and adsorption of water molecules proceeded smoothly, and a large number of active sites were induced to participate in the reaction.

Encouraged by the outstanding bi-functional OER/HER activity of these catalytic electrodes, an iR correction-free practical alkaline water electrolyzer for overall water splitting was evaluated with a

two-electrode configuration. As shown in Fig. 3e, the current density of the water electrolyzer with two NiBMP@N$_x$C catalytic electrodes increased drastically according to the anodic sweep of the applied potential, with an applied potential of 1.46 V at j = 20 mA cm^{-2} and 1.65 V at j = 100 mA cm^{-2}. Notably, an asymmetric water electrolyzer composed of Ir/C(+)//Pt/C(-) electrodes required a much larger voltage (1.56 V at j = 20 mA cm^{-2} and 1.77 V at j = 100 mA cm^{-2}) to produce the same current as compared to a symmetric configuration consisting of two pieces of NiBMP@N$_x$C electrode. The durability of this overall water splitting cell was tested using the chronoamperometric technique with applied voltages of 1.47 and 1.65 V to produce 20 and 100 mA cm^{-2} of current density, respectively, and the results are shown in Fig. 3f. The NiBMP@N$_x$C based water electrolyzer showed very good durability, with over ~ 95 % retention of the current after 28 h operation.

Next, the catalytic activities of the NiBIF-derived samples toward ORR were also evaluated to investigate the tri-functional catalytic activity. Of the various ZIF-67-derived nanomaterials, the Co-N$_x$-C carbon material is proven to be highly active toward ORR. Therefore, the detailed nanostructure and chemical composition of NiBM@N$_x$C was further investigated before the ORR characterization. Fig. 4a shows the SEM image of the typical NiBM@N$_x$C, which is detached from nickel foam. In Fig. 4c, the detailed nanostructure of the NiBM@N$_x$C can be observed composed of numerous short carbon nanotubes, which were grown *in-situ* in the annealing process in the presence of cobalt/nickel metallic nanoparticles. The nanostructure was further investigated with TEM analysis as shown in Fig. 4b. The surface of NiBM@N$_x$C was found to be surrounded by the as-grown carbon nanotubes. In the HR-TEM image in Fig. 4d, highly graphitic carbon nanocages encapsulating metallic nickel-cobalt nanoparticles were observed. The STEM image and the elemental mapping images of the corresponding Ni, Co, C and N are illustrated in Fig. 4e. Each element was found to be well-distributed throughout the whole NiBM@N$_x$C nanocrystal. In the PXRD pattern of the NiBM@N$_x$C (Fig. S18), the presence of nickel-cobalt particles was confirmed along with a strong peak at 26° corresponding to the (002) plane of the graphitic carbon peak. The overall XPS spectra (Fig. 4f) provided evidence for the presence of C, N, Co and Ni elements. In the fine Ni 2p spectra (Fig. S19a), the strong peak at 852.4 eV coincides with Ni in the zer-valence state, and in the fine Co 2p spectra (Fig. S19b), a peak at 779.1 eV corresponding to Co in the zero-valence state was also observed. The metal species in the MOF can be partially reduced through the annealing process, and transition-metal nanoparticles are known to catalyze the *in-situ* growth of carbon nanotubes.[30] The high-resolution XPS spectra for N 1s was deconvoluted into 4 different nitrogen peaks at 398.9, 400.4, 401.3 and 403.8 eV, corresponding to pyridinic, pyrollic, graphitic, and oxidized nitrogen species, respectively.[48] The physical N$_2$ absorption experiments revealed the detailed nanostructure, as shown in Fig. 4g, and the specific surface area was 545 and 1102 m^{2}g^{-1} for NiBMP@N$_x$C and NiBM@N$_x$C. The corresponding inset image of pore size distribution obtained with density functional theory (DFT) based modeling shows that additional nanopores appeared for the NiBM@N$_x$C. These were attributed to the presence of carbon nanotubes and hollow carbon nanospheres, as confirmed in the HR-TEM images.
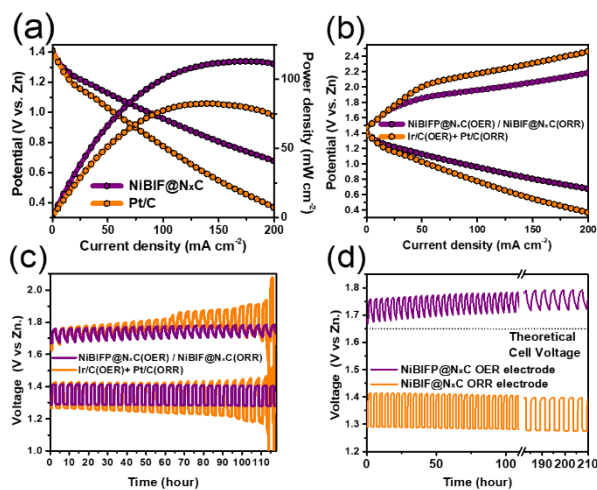
Figure 6. (a) Polarization and the corresponding power density curves of the primary ZABs for Pt/C (orange) and NiBM@N$_x$C (purple). (b) Discharge and charge polarization curves of Pt/C + Ir/C (orange) and NiBM@N$_x$C + NiBMP@N$_x$C (purple) air electrodes for the rechargeable ZABs. (c) Discharge and charge voltage profiles of ZABs with Ir/C + Pt/C (orange) and NiBMP@N$_x$C + NiBM@N$_x$C (purple) decoupled catalysts at a current density of 10 mA cm^{-2} at ambient temperature. (d) The cyclic stability of the rechargeable ZABs with NiBM@N$_x$C/NiF (ORR, orange) + NiBMP@N$_x$C/NiF (OER, purple) electrodes for a period of ~ 210 h. The current density is 10 mA cm^{-2}, and the electrolyte is 6 M KOH with 0.2 M ZnCl$_2$ solution.

The ORR catalytic activity of the NiBIF-derived samples and Pt/C was first evaluated in O$_2$-saturated 0.1 M KOH solution loaded onto a glassy carbon electrode with a rotating ring-disk electrode experiments (RRDE) configuration. As shown in the CV curves (Fig. 5a), the cathodic peak position of NiBM-O was greatly shifted to anodic direction by the introduction of N-doped carbon matrix. Furthermore, the cathodic peak of NiBM@N$_x$C (0.87 V) was close to that of Pt/C, indicating the high intrinsic ORR activity. LSV measurements were carried out in O$_2$-saturated 0.1 M KOH solution at a rotating speed of 1600 rpm with a scan rate of 1 mV s^{-1}. As shown in Fig. 5b, the ORR activity of NiBM-O is poor in the absence of N-doped carbon matrix. NiBMP@N$_x$C shows a relatively high diffusion-limiting current density of 4.6 mA cm^{-2} and a half wave potential at 0.82 V vs. RHE. Furthermore, NiBM@N$_x$C exhibits the highest ORR activity (j$_{l.m}$=5.92 mA cm^{-2}, V$_{half}$ = 0.88 V$_{RHE}$), which is close to that of Pt/C (jl.m=5.78 mAcm^{-2}, V$_{half}$ = 0.89 V$_{RHE}$). The multiple catalytic activity of these tunable tri-functional catalysts also outperforms most of the recently developed bifunctional electrocatalysts for metal-air batteries[25, 28, 49-52] (Table S3) as well as tri-functional electrocatalysts toward HER/OER/ORR[21-23, 25, 26] (Table S4). The Tafel slope of NiBM@N$_x$C is 47.6 mV dec^{-1}, which is much smaller than that of the other samples including Pt/C (76.6 mV dec^{-1}), as shown in Fig. S20a. From the RRDE-based LSV curves of each catalyst (Fig. S20b), the electron transfer number and the hydrogen peroxide yield can be calculated, as shown in Fig. 5c. The percentage of HO$_2^-$ generated on NiBM@N$_x$C and Pt/C catalyst is below 10%, and the corresponding electron transfer number for NiBM@N$_x$C is 3.76 - 3.97, which is quite close to that of Pt/C (3.87 – 3.99). The durability of the NiBM@N$_x$C catalyst for the ORR reaction was verified by LSV measurement after 10,000 cycles of CV between 1.0 and 1.6 V$_{RHE,}$ versus the LSV curve before the CV cycling (Fig. 5d). By comparing the LSV curves, the half-wave potential difference before and after the durability test was found to be only 12 mV. The high durability of these catalysts is believed to be due to the presence of a particularly high-quality graphitic carbon matrix. On the other hand, the Pt/C catalyst showed a much greater reduction in catalytic activity with a half-wave potential shift of ~ 34 mV compared to the NiBM@N$_x$C catalyst (Fig. S21).

On the other hand, the precipitated NiBM hydroxide obtained by a hydrothermal reaction was also used to investigate the possibility of mass production. The NiBM hydroxide precipitate was collected and processed into an ORR catalytic material through the same procedure as above. It was confirmed that NiBM hydroxide precipitate synthesized through the hydrothermal reaction at 180 °C had a sea urchin-shaped nanostructures with an average size of several micrometers (Fig. S22a,c). For the conversion reaction to NiBIF, the precipitate was immersed in MIM solution and stored in an electric oven at 25, 40, 60, and 80 °C for 8 h each. For samples that were reacted at 25° C, very small NiBIF nanocrystals were found to grow on the existing nanowire surfaces (Fig. S22b,d). Again, as the reaction progressed at high temperatures, it was observed that the size of the NiBIF nanocrystals increased and interconnectivity improved, as shown in Fig. S23a-h. For the sample processed at the highest temperature of 80 °C (Fig. S23d,h), several micrometer-sized precipitate surfaces were observed to be completely covered with interconnected NiBIF nanostructures. The colors of the ZIF-67 and NiBIF precipitates were blue and green-brown, respectively (Fig. S24). The XPS survey spectra of the NiBIF precipitates showed a pattern similar to the sample grown directly on the nickel foam (Fig. S25). The NiBIF precipitate was also directly converted to a bimetal-nitrogen doped carbon catalyst (denoted as NiBM@N$_x$C-X, where X = 40, 60, 80, which indicates the temperature in the second-step conversion reaction) through the annealing process in an argon atmosphere. By comparison, the untreated Ni-BM hydroxide were severely aggregated and had lost their original nanostructures after the annealing process at 800 °C for 3 h in an argon flow (Fig. S26a,b). In contrast, the overall original shape of the NiBM@N$_x$C sample was well preserved, providing the strong evidence of successful incorporation of carbon species. In Fig. S27a-d, NiBM@N$_x$C-80 with several micrometers in size were observed to have a hierarchical nanostructure of metal-carbon composite nanofibers. Another control sample of NiBM@N$_x$C-60 exhibited a hierarchical fiber-like interconnected nanostructure, as shown in the SEM images (Fig. S28a,d), and the detailed nanostructure can be observed in the TEM images (Fig. S28b,e). The nanofibers were found to consist of hollow carbon nanospheres or core-shell structures in which nickel-cobalt nanoparticles are encapsulated in nanocages (Fig. S28c, f). Similarly, the ZIF-67 precipitates (Fig. S29a) were also successfully converted to ZIF-67-N$_x$C (Fig. S29b) through an identical annealing process. The ORR catalytic activity of the NiBM@N$_x$C samples was also evaluated. As shown in the CV curves carried out in O$_2$-saturated 0.1 M KOH solution (Fig. S30a), the apparent cathodic peaks were observed for all three samples, and the highest cathodic peak was observed for

ARTICLE

NiBM@N$_x$C-40. From the LSV curves (Fig. S30b), the diffusion-limited current density and the half-wave potential of three samples were similar (J$_{l.m}$= 5.2-5.3 mA cm^{-2}, V$_{half}$ = 0.86-0.87 V vs.RHE). The Tafel slopes of the NiBM@N$_x$C catalyst extracted from the Tafel plot in Fig. S29c also exhibit relatively lower values (45.7-62.1 mV dec^{-1}), indicating the favorable ORR activity owing to the successful formation of M-N-C active sites as well as the hierarchical nanostructure. As shown in Fig. S30d, the hydrogen peroxide yield and electron transfer number were calculated from the LSV curves of RRDE (Fig. S31). Again, electron transfer numbers close to 4 and less than 10% hydrogen peroxide were observed, which are similar to those of Pt/C catalyst. The LSV curves measured with increasing rotation rate can be observed in Fig. S32a-d, and a Koutechy-Levich (K-L) plot can be derived from the limiting current density of the LSV curves (Fig. S32a-d, inset). The LSV curves and corresponding K-L plots for all of the NiBM@N$_x$C catalysts reveal ideal electron transfer number values close to 4 for the evaluated catalysts.

Finally, rechargeable zinc-air batteries with a three-electrode configuration were assembled, composed of a zinc anode and two decoupled air electrodes for OER and ORR. Two pieces of NiBIF electrode were converted into a NiBMP@N$_x$C OER electrode and a NiBM@N$_x$C ORR electrode, and they exhibited high catalytic activity in each reaction. In Fig. 6a, the polarization curve and the power density of the primary ZABs was observed. In the discharge polarization curves, the Pt/C catalyst initially exhibited better electrochemical performance than the NiBM@N$_x$C. However, the NiBM@N$_x$C showed a power density of 113 Wcm^{-2}, which is much higher than that of the Pt/C catalyst (82.4 Wcm^{-2}) at high current densities. In the charge and discharge polarization curves of the rechargeable ZABs (Fig. 6b), the non-precious metal catalysts based ZABs (NiBM@N$_x$C ORR electrode + NiBMP@N$_x$C OER electrode) exhibited much lower overpotential compared to the counterparts of precious metal-based ZABs (Pt/C ORR electrode + Ir/C OER electrode). At the relatively high ZABs current density of 10 mA cm^{-2} appropriate for more practical applications, the non-precious metal catalysts-based ZABs exhibited extremely low overpotential and very stable cycle performance up to 120 h. However, the original good cyclic performances of the precious metal catalyst-based ZABs gradually diminished, resulting in a significant increase in overpotential during the charge-discharge cycle of this condition, with relatively high current density and high applied overpotentials. These results suggest that the NiBIF-based catalytic electrode, which stably supports the catalytic material due to its excellent electrode adhesion, can maintain a very stable cycle performance during high power density ZABs operation, suitable for commercialization.

The ZABs with the NiBIF-based catalytic electrodes exhibited very good cyclic performance and durability over a period of about 210 h in a galvanostatic cyclic test at 10 mA cm^{-2} (Fig. 6d). This cyclic behavior of the non-precious metal catalyst-based batteries can be explained by the characteristics of the bulk-type catalytic electrodes, which require low overvoltages, especially to produce high current densities. Currently, our group is conducting research to fabricate nickel-rich bimetallic-imidazolate framework under milder conditions. To synthesize the nickel-rich nickel-cobalt nanostructure, two metal ions are mixed at a desired molar ratio in the growth solution and reacted at 90 $^{\circ}$C, followed by the conversion reaction to produce nickel-rich bimetallic-imidazolate framework. The resultants have exhibited different colors as the molar ratio of nickel to cobalt was varied. (Pictures in Fig. S33 show the precipitates solution, and the pictures in Fig. S34 show the nanomaterials directly grown on nickel foam). The nickel-cobalt nanowires (Fig. S35a-c) were found to be successfully converted to bimetallic-imidazolate framework nanocrystals (Fig. S35d-f) after the conversion reaction at 40 $^{\circ}$C.

Conclusion

In summary, the novel approach presented here produces a nickel-cobalt bimetallic-imidazolae framework with a hierarchical rather than a conventional ZIF-67 simple structure. The hierarchical metal-organic complex can be grown directly on nickel foam to produce bulk catalytic electrodes and can also be produced as catalyst nanomaterials in powder form using precipitates. Due to the complex characteristics, a high quality carbon nanocage is formed during the annealing process, and each catalyst nanoparticle is encapsulated in an isolated state. Owing to these rational nanostructures and high adhesion due to the direct-growth strategy of complex catalysts, these two types of catalytic electrodes exhibited excellent tri-functional activity and durability. This new approach to the mass production of efficient multi-functional catalysts with abundant and inexpensive raw materials is expected to accelerate the commercialization of diverse energy conversion and storage systems that require an electrocatalyst.

Acknowledgements

Notes and references

1.   L. Schlapbach, *Nature*, 2009, **460**, 809.
2.   J. Wang, F. Xu, H. Jin, Y. Chen and Y. Wang, *Adv. Mater.*, 2017, **29**, 1605838-n/a.
3.   M. S. Faber and S. Jin, *Energy Environ. Sci.*, 2014, **7**, 3519-3542.
4.   C. C. L. McCrory, S. Jung, J. C. Peters and T. F. Jaramillo, *J. Am. Chem. Soc.*, 2013, **135**, 16977-16987.
5.   Z. W. Seh, J. Kibsgaard, C. F. Dickens, I. B. Chorkendorff, J. K. Norskov and T. F. Jaramillo, *Science*, 2017, **355**.
6.   J. Ahmed, A. Ganguly, S. Saha, G. Gupta, P. Trinh, A. M. Mugweru, S. E. Lofland, K. V. Ramanujachary and A. K. Ganguli, *J. Phys. Chem. C*, 2011, **115**, 14526-14533.
7.   J. Ahmed, B. Kumar, A. M. Mugweru, P. Trinh, K. V. Ramanujachary, S. E. Lofland, Govind and A. K. Ganguli, *J. Phys. Chem. C*, 2010, **114**, 18779-18784.
8.   J. Ahmed, T. Ahamad and S. M. AlShehri, *ChemElectroChem*, 2017, **4**, 1222-1226.

9. J.-I. Jung, M. Risch, S. Park, M. G. Kim, G. Nam, H.-Y. Jeong, Y. Shao-Horn and J. Cho, *Energy Environ. Sci.*, 2016, **9**, 176-183.

10. Y. Zhu, W. Zhou, Y. Zhong, Y. Bu, X. Chen, Q. Zhong, M. Liu and Z. Shao, *Adv. Energy Mater.*, 2016, **7**.

11. X. Zhong, Y. Jiang, X. Chen, L. Wang, G. Zhuang, X. Li and J.-g. Wang, *J. Mater. Chem. A*, 2016, **4**, 10575-10584.

12. S. H. Ahn and A. Manthiram, *J. Mater. Chem. A*, 2017, **5**, 2496-2503.

13. X. Xiao, C.-T. He, S. Zhao, J. Li, W. Lin, Z. Yuan, Q. Zhang, S. Wang, L. Dai and D. Yu, *Energy Environ. Sci.*, 2017, **10**, 893-899.

14. Y. Hou, M. R. Lohe, J. Zhang, S. Liu, X. Zhuang and X. Feng, *Energy Environ. Sci.*, 2016, **9**, 478-483.

15. S. Dou, L. Tao, J. Huo, S. Y. Wang and L. M. Dai, *Energy Environ. Sci.*, 2016, **9**, 1320-1326.

16. J. Zhang, Z. Zhao, Z. Xia and L. Dai, *Nature Nanotech.*, 2015, **10**, 444.

17. H. Sun, Y. Lian, C. Yang, L. Xiong, P. Qi, Q. Mu, X. Zhao, J. Guo, Z. Deng and Y. Peng, *Energy Environ. Sci.*, 2018, DOI: 10.1039/C8EE00934A.

18. Z. X. Pei, H. F. Li, Y. Huang, Q. Xue, Y. Huang, M. S. Zhu, Z. F. Wang and C. Y. Zhi, *Energy Environ. Sci.*, 2017, **10**, 742-749.

19. C. S. Lim, C. K. Chua, Z. Sofer, K. Klímová, C. Boothroyd and M. Pumera, *J. Mater. Chem. A*, 2015, **3**, 11920-11929.

20. C. Hu and L. Dai, *Adv. Mater.*, 2017, **29**, 1604942.

21. J. T. Zhang and L. M. Dai, *Angew. Chem. Int. Ed.*, 2016, **55**, 13296-13300.

22. Y. Jia, L. Z. Zhang, A. J. Du, G. P. Gao, J. Chen, X. C. Yan, C. L. Brown and X. D. Yao, *Adv. Mater.*, 2016, **28**, 9532-+.

23. X. Zhang, R. Liu, Y. Zang, G. Liu, G. Wang, Y. Zhang, H. Zhang and H. Zhao, *Chem. Commun.*, 2016, **52**, 5946-5949.

24. S. M. Alshehri, A. N. Alhabarah, J. Ahmed, M. Naushad and T. Ahamad, *J. Colloid Interface Sci.*, 2018, **514**, 1-9.

25. H. Li, Q. Li, P. Wen, T. B. Williams, S. Adhikari, C. Dun, C. Lu, D. Itanze, L. Jiang, D. L. Carroll, G. L. Donati, P. M. Lundin, Y. Qiu and S. M. Geyer, *Adv. Mater.*, 2018, DOI: 10.1002/adma.201705796, 1705796-n/a.

26. T. Meng, J. W. Qin, S. G. Wang, D. Zhao, B. G. Mao and M. H. Cao, *J. Mater. Chem. A*, 2017, **5**, 7001-7014.

27. X. Xu, H. F. Liang, F. W. Ming, Z. B. Qi, Y. Q. Xie and Z. C. Wang, *ACS Catal.*, 2017, **7**, 6394-6399.

28. D. N. Ding, K. Shen, X. D. Chen, H. R. Chen, J. Y. Chen, T. Fan, R. F. Wu and Y. W. Li, *ACS Catal.*, 2018, **8**, 7879-7888.

29. T. T. Wang, Z. K. Kou, S. C. Mu, J. P. Liu, D. P. He, I. S. Amiinu, W. Meng, K. Zhou, Z. X. Luo, S. Chaemchuen and F. Verpoort, *Adv. Funct. Mater.*, 2018, **28**.

30. B. Y. Xia, Y. Yan, N. Li, H. B. Wu, X. W. Lou and X. Wang, *Nature Energy*, 2016, **1**.

31. H. Zhou, F. Yu, Q. Zhu, J. Sun, F. Qin, Y. Luo, J. Bao, Y. Yu, S. Chen and Z. Ren, *Energy Environ. Sci.*, 2018, DOI: 10.1039/C8EE00927A.

32. J. Zhou, Y. B. Dou, A. Zhou, R. M. Guo, M. J. Zhao and J. R. Li, *Adv. Energy Mater.*, 2017, **7**, 1602643.

33. P. Falcaro, K. Okada, T. Hara, K. Ikigaki, Y. Tokudome, A. W. Thornton, A. J. Hill, T. Williams, C. Doonan and M. Takahashi, *Nature Mater.*, 2017, **16**, 342-348.

34. D. Yu, B. Wu, L. Ge, L. Wu, H. Wang and T. Xu, *J. Mater. Chem. A*, 2016, **4**, 10878-10884.

35. D. Yu, B. Wu, J. Ran, L. Ge, L. Wu, H. Wang and T. Xu, *J. Mater. Chem. A*, 2016, **4**, 16953-16960.

36. I. B. Vasconcelos, T. G. d. Silva, G. C. G. Militao, T. A. Soares, N. M. Rodrigues, M. O. Rodrigues, N. B. d. Costa, R. O. Freire and S. A. Junior, *RSC Advances*, 2012, **2**, 9437-9442.

37. Y. Feng, X.-Y. Yu and U. Paik, *Chem. Commun.*, 2016, **52**, 1633-1636.

38. L. Yan, L. Cao, P. Dai, X. Gu, D. Liu, L. Li, Y. Wang and X. Zhao, *Adv. Funct. Mater.*, 2017, **27**, 1703455-n/a.

39. P. He, X. Y. Yu and X. W. Lou, *Angew. Chem. Int. Ed.*, 2017, **56**, 3897-3900.

40. X. Xiao, C.-T. He, S. Zhao, J. Li, W. Lin, Z. Yuan, Q. Zhang, S. Wang, L. Dai and D. Yu, *Energy Environ. Sci.*, 2017, **10**, 893-899.

41. S. Dresp, F. Luo, R. Schmack, S. Kühl, M. Gliech and P. Strasser, *Energy Environ. Sci.*, 2016, **9**, 2020-2024.

42. X. Lu and C. Zhao, *Nat. Commun.*, 2015, **6**, 6616.

43. L. Yu, H. Zhou, J. Sun, F. Qin, F. Yu, J. Bao, Y. Yu, S. Chen and Z. Ren, *Energy Environ. Sci.*, 2017, **10**, 1820-1827.

44. Y. Liu, Q. Li, R. Si, G.-D. Li, W. Li, D.-P. Liu, D. Wang, L. Sun, Y. Zhang and X. Zou, *Adv. Mater.*, 2017, **29**, 1606200-n/a.

45. J. Jiang, Q. X. Liu, C. M. Zeng and L. H. Ai, *J. Mater. Chem. A*, 2017, **5**, 16929-16935.

46. X. D. Wang, H. Y. Chen, Y. F. Xu, J. F. Liao, B. X. Chen, H. S. Rao, D. B. Kuang and C. Y. Su, *J. Mater. Chem. A*, 2017, **5**, 7191-7199.

47. C. Ray, S. C. Lee, B. J. Jin, A. Kundu, J. H. Park and S. C. Jun, *J. Mater. Chem. A*, 2018, **6**, 4466-4476.

48. W. Zhang, Z.-Y. Wu, H.-L. Jiang and S.-H. Yu, *J. Am. Chem. Soc.*, 2014, **136**, 14385-14388.

49. W. Niu, S. Pakhira, K. Marcus, Z. Li, J. L. Mendoza-Cortes and Y. Yang, *Adv. Energy Mater.*, 2018, **8**, 1800480.

50. Y. Jiang, Y.-P. Deng, J. Fu, D. U. Lee, R. Liang, Z. P. Cano, Y. Liu, Z. Bai, S. Hwang, L. Yang, D. Su, W. Chu and Z. Chen, *Adv. Energy Mater.*, 2018, **8**, 1702900.

51. Y. N. Chen, Y. B. Guo, H. J. Cui, Z. J. Xie, X. Zhang, J. P. Wei and Z. Zhou, *J. Mater. Chem. A*, 2018, **6**, 9716-9722.

52. Q. C. Wang, Y. P. Lei, Z. Y. Chen, N. Wu, Y. B. Wang, B. Wang and Y. D. Wang, *J. Mater. Chem. A*, 2018, **6**, 516-526.

Graphical Abstract

Hierarchical Tri-functional Electrocatalysts Derived from Bimetallic-imidazolate Framework for Overall Water Splitting and Rechargeable Zinc-air Batteries

Due to the hierarchical structure resulting from the transformation to the bimetallic-imidazolate framework, this catalyst electrode has a benchmarking tri-functional catalytic activity.